Research Article Vol. 4, No. 5 / 15 May 2021 / OSA Continuum 1497

Influence of surface and interface roughness on X-ray and extreme ultraviolet reflectance: A comparative numerical study

YUKA ESASHI,[1,*] MICHAEL TANKSALVALA,[1] ZHE ZHANG,[1,2] NICHOLAS W. JENKINS,[1] HENRY C. KAPTEYN,[1,3] AND MARGARET M. MURNANE[1]

[1] *STROBE Science and Technology Center and JILA, University of Colorado Boulder, Colorado 80309, USA*
[2] *MOE Key Laboratory of Advanced Microstructural Materials, Institute of Precision Optical Engineering, School of Physics Science and Engineering, Tongji University, Shanghai 20092, China*
[3] *KMLabs Inc., 4775 Walnut St. Building 102, Boulder, Colorado 80301, USA*
[*] *yuka.esashi@colorado.edu*

Abstract: The influence of surface and interface roughness on X-ray and extreme ultraviolet (EUV) reflectometry is becoming increasingly important as layer thicknesses decrease to a few nanometers in next-generation nanodevices and multilayer optics. Here we simulate two different approaches for numerically modeling roughness, the Névot–Croce factor and the graded-interface method, in the Parratt formalism of calculating the complex reflectance of multilayer systems. The simulations were carried out at wavelengths relevant to widely used metrology techniques, including 0.154 nm for X-ray reflectometry and 13.5 nm for EUV lithography. A large discrepancy is observed between the two approaches in several situations: when the roughness is large with respect to the wavelength, for interfaces with large changes in refractive index across the boundary, as well as around reflectance peaks due to interference effects. Caution is thus required when using either approach to model roughness in these situations.

1. Introduction

The performance of next-generation semiconductor and quantum devices increasingly relies on intricately designed multilayer structures, with layer thicknesses of only a few nanometers in some cases. In these situations, even small amounts of surface and interface roughness of ~0.1–1 nm become comparable to the layer thicknesses and can introduce non-negligible effects to the device characteristics. Surface and interface roughness have been shown to affect the performance of various systems, including metal–oxide–semiconductor field-effect transistors (MOSFETs) [1,2], extreme ultraviolet (EUV) lithography photomasks [3,4], quantum wells [5], and magnetic multilayer systems [6–8]. Going forward, it is expected that even more properties of future devices will be surface- and/or interface-dominated. Therefore, for successful development of new devices, it is crucial that the effect of surface and interface roughness is correctly accounted for both in simulations and experimental data analysis.

X-ray and EUV reflectometry techniques (XRR, EUVR) are commonly used to probe multilayer systems because of their high sensitivity to small length-scale features as well as their intrinsic elemental and chemical specificity [9–17]. By measuring the X-ray or EUV reflectance of samples as a function of angle of incidence, and then optimizing a numerical model of the sample until the predicted reflectance curve matches the experimental data, it is possible to solve for the depth-dependent structure parametrized by chemical composition, layer thicknesses and surface/interface roughness. To achieve good control over the illumination used for XRR and EUVR, super-polished optics and high-quality multilayer mirrors are crucial, and their quality control also often relies heavily on reflectometry techniques [18–20]. Therefore, correct modeling

#422924 https://doi.org/10.1364/OSAC.422924
Journal © 2021 Received 1 Mar 2021; revised 16 Apr 2021; accepted 17 Apr 2021; published 3 May 2021

OSA CONTINUUM

of roughness is important for device metrology not only when analyzing devices by XRR and EUVR, but also to facilitate manufacturing of high-quality optics.

The X-ray and EUV specular reflectance from transversely uniform regions of multilayer structures is often modeled using the Parratt formalism, which uses Fresnel coefficients at each interface in a recursive computation [21–23]. Since Fresnel coefficients are defined for ideal and perfectly flat interfaces, the effect of roughness is usually accounted for using the Névot–Croce factor [24,25], which corrects the Fresnel coefficient of an interface according to its roughness. However, there also exists an alternative approach for taking roughness into account that is also compatible with the Parratt formalism; in this approach, a rough interface is modeled in a transversely averaged way, by representing it as a gradual change in the refractive index using many thin layers, each of which has a constant refractive index [26]. While multiple authors have credited this graded-interface approach (sometimes called the slide method) as being more accurate, it has often been criticized for being too computationally intensive [10,27]. However, given the recent rapid increase in computational power, it is timely to explore a more comprehensive comparison of the performance of the Névot–Croce factor against the graded-interface approach. In particular, if there is any significant discrepancy between the simulated reflectance from the two approaches, then at least one of the approaches must be inaccurate, and some caution is required in using either of them.

In this paper, we compare the Névot–Croce factor against the graded-interface approach in areas that have not been fully investigated before, namely for EUV wavelengths, for simulating phase shifts upon reflection, and for characterizing multilayer systems. In the following sections, we first explain the motivation for investigating these three particular areas. Next, we provide a brief overview of the Névot–Croce factor and the graded-interface approach and offer guidance on how best to implement the graded-interface approach. Then, for the remainder of the paper, we compare simulated reflectance using the Névot–Croce factor and the graded-interface approach for three different scenarios: a bulk substrate, a monolayer, and a multilayer system. These comparisons are done for both X-ray and EUV wavelengths, for both the amplitude and phase of reflectance, and for both S- and P-polarizations when appropriate. Finally, we provide recommendations for when care is needed in choosing between the two approaches.

2. Areas of comparison

In this paper, we cover three areas where the comparison of the Névot–Croce factor against graded-interface approach that is discussed in the literature is insufficient.

The first area is comparing the two approaches for EUV wavelengths. EUVR is a relatively new metrology technique, which has relied on roughness modeling studies from XRR and neutron reflectometry. For probing similar degrees of roughness, EUV reflectance is expected to be less affected than X-ray reflectance given the longer EUV wavelengths. However, many materials are reflective to EUV wavelengths over a larger range of incident angles — not just at the grazing incidence angles required for XRR. Therefore, it is worth exploring how the two roughness modeling approaches agree for the larger incidence angles (from grazing) that can be accessed at EUV wavelengths.

The second area we explore is in simulating the phase shift upon reflection. While traditional reflectometry schemes use intensity reflectance measurements made using incoherent X-ray light, recent developments in coherent X-ray and EUV sources using synchrotrons, free-electron lasers and high harmonic generation sources [28,29], together with phase-sensitive techniques such as coherent diffractive imaging, are enabling accurate and quantitative measurements of the phase shift upon reflection [30–33]. The phase shift is often more sensitive to topography and material composition than the intensity reflectance [33], so it is very possible that more XRR- and EUVR-related techniques will harness phase measurements in the future. In addition, the phase shift is sometimes an important parameter that requires optimization in the design of EUV

OSA CONTINUUM

optics, or photomasks used in EUV lithography [34]. Therefore, accurately modeling the phase shift upon reflection for X-rays and EUV light is becoming more critical for the community; however, the current literature on this topic is quite limited [35,36]. In fact, it is known that for a surface with a roughness distribution of $1/\cosh^2(z/\sigma)$ as a function of depth z and parametrized by degree of roughness σ, the approximated solution for reflectance from a rough surface using the distorted-wave Born approximation (DWBA; equivalent to the approximation made in the derivation of the Névot–Croce factor) differs from the exact theoretical solution by a phase factor [35–37]. While this discrepancy has often been neglected to date due to its small size and difficulty of measurement, it is worthwhile to revisit this discrepancy, since quantitative phase-sensitive reflection measurements are now gaining in utility.

The third area we explore is thin-film and multilayer systems. This area is particularly interesting in light of the ever-reducing layer thicknesses in these systems. It is now common to have interface roughness that are comparable to the layer thickness. It has been suggested that the graded-interface approach is more suitable than the Névot–Croce factors in this scenario [38], and in addition it has been shown that the field strength calculated very close to the center of an interface using the Névot–Croce factor is not correct [39]. This error may cascade and manifest with greater magnitude if interfaces are located close to each other.

An additional topic that is also poorly covered in the literature is calculation of the transmissivity and the associated phase shift from a system with rough surfaces [36]. However, here we limit our discussion to reflection, since the majority of thin-film measurements are done in reflection.

3. Névot–Croce factor

The Névot–Croce and Debye–Waller factors correct the Fresnel coefficients of an interface according to its roughness. The former is used for approximating the effect of roughness that has high transverse spatial frequency, where diffuse scattering is negligible. The latter is used for roughness with low transverse spatial frequency, where diffuse scattering is located very close to the specular reflection. The Névot–Croce factor corrects the reflection and transmission Fresnel coefficients of an interface with a normally distributed roughness with RMS of σ by the following factors [10,24,26]:

$$\begin{aligned} \text{Reflection}: &\ \exp(-2k_{i,z}k_{j,z}\sigma^2) \\ \text{Transmission}: &\ \exp((k_{i,z}-k_{j,z})^2\sigma^2/2), \end{aligned} \tag{1}$$

where $k_{i,z}$ and $k_{j,z}$ are the component of the wave vector that are perpendicular to the interface, in the medium before and after the interface respectively, with $k = 2\pi n/\lambda_0$ where n is the refractive index of the medium and λ_0 is the wavelength of the light in vacuum, and $k_z = k \sin\theta$ where θ is the propagation angle in the medium measured from grazing. The Debye–Waller factor similarly corrects the Fresnel coefficients by the following [10,39]:

$$\begin{aligned} \text{Reflection}: &\ \exp(-2k_{i,z}^2\sigma^2) \\ \text{Transmission}: &\ \exp(-(k_{i,z}-k_{j,z})^2\sigma^2/2). \end{aligned} \tag{2}$$

The approximation used in the derivation of these factors is valid in the region $\sigma k_{i,z} < 1$ [40], and when there is only a small difference in the refractive index of the media separated by the interface (which is often true for X-rays and EUV wavelengths where the refractive index is usually very close to unity) [41]. Using the first constraint, for example, for wavelength of 0.154 nm at 5° from grazing entering from a medium with refractive index of 1, we must have $\sigma < 0.28$ nm, and for wavelength of 13.5 nm at 30° from grazing, we must have $\sigma < 4.3$ nm. It should be noted that in general, and especially for X-ray and EUV wavelengths, the refractive index

OSA CONTINUUM

of most materials is complex; this means that both k and θ (calculated using Snell's law with complex refractive indices) and therefore k_z are complex, and as a result, the Névot–Croce and Debye–Waller factors are also correspondingly complex, and thus modify both the amplitude and the phase of Fresnel coefficients.

To express the operating regimes of Névot–Croce and Debye–Waller factors more mathematically, consider a simple grating of period Λ, and an incident beam at a grazing angle of θ. The m^{th}-order diffraction maximum is observed at angle θ_m from grazing where the grating equation $m\lambda = \Lambda\,(\cos\theta_m - \cos\theta)$ is satisfied, where λ is the wavelength of the light. If $\Lambda < \lambda/(1 - \cos\theta)$, then the first diffraction order does not exist (i.e., there is negligible diffraction, at least on the side of the reflected beam closest to the sample surface). Therefore, if the correlation length ξ (roughly defined as the largest period in the transverse roughness profile) satisfies $\xi \ll \lambda/(1 - \cos\theta)$, diffuse scattering will be small and the Névot–Croce factor may be used. Conversely, if $\xi \gg \lambda/(1 - \cos\theta)$, then diffuse scattering is not very angularly separated from the specular reflection and the Debye–Waller factor may be used [39]. For most systems investigated under XRR or EUVR, the roughness has a relatively short correlation length (for example, polished Si wafers have a correlation length of about 1 μm [42], and metal-coated fused quartz have a correlation length of 100–200 nm [43]), therefore the Névot–Croce is the more commonly used factor. Also, as shown in Figs. 15 to 18 of the appendix, the two factors are similar for roughness less than 1 nm, and the greatest discrepancy is restricted to the region of total external reflection. Therefore, in this paper we focus on the Névot–Croce factor.

The Névot–Croce and Debye–Waller factors have been derived using multiple approaches, most notably using the DWBA [41,44,45]. A more general theory that bridges the two correlation length regimes [45], as well as higher-order corrections to the Névot–Croce factor [36,46,47] have previously been suggested, however the most basic forms in Eq. (1) and (2) are often used for their computational simplicity. There are multiple software programs that are publicly available for the purposes of calculating X-ray and EUV reflectance, including IMD [22], GenX [48], REFLEX [49], JGIXA [50], MOTOFIT [51], and refnx [52], and the most commonly used method for taking account of surface/interface roughness in these programs is the Névot–Croce factor.

4. Graded-interface approach

In the graded-interface approach, a rough interface is represented as a gradual change in the refractive index using many thin layers, each with a constant refractive index [26].

It is important to point out that there are two ways in which an interface may deviate from a perfectly smooth interface. One is where the interface is rough but there is no mixing — meaning the interface is affected by the morphological characteristics of the boundary. The second is where there is interdiffusion of chemicals across the interface at the atomic or molecular level. The graded-interface approach makes a direct physical representation of the latter type of interfaces, and a transversely averaged representation of the first type of interfaces.

While some of the software programs available for calculation of X-ray reflectance are capable of running the graded-interface approach (including IMD [22]), users may choose to write their own version as the pre-existing programs may not offer all the necessary functionalities. In this section, we cover two ways in which one might implement the graded-interface approach to model surface/interface roughness. Though there are certainly other possible implementations, we find that these two serve most purposes, with the choice between the two offering a tradeoff between flexibility and computational speed.

The two implementations we will describe are illustrated in Fig. 1. As shown in Fig. 1(a), to describe roughness at an interface, it is important to know the topographic distribution of the surface and the corresponding profile that the gradient of the refractive index takes, defined by a function shape and a characteristic width. As shown in Fig. 1(b), for both the Névot–Croce factor and the graded-interface approach, the process starts from the description of the multilayer stack

OSA CONTINUUM

to be simulated, parametrized by layer thicknesses, refractive indices, and the roughness at each of the interfaces. In both implementations of the graded-interface approach that we discuss, the final model is a discretized refractive index profile as a function of depth that can then be fed into a Parratt formalism calculator.

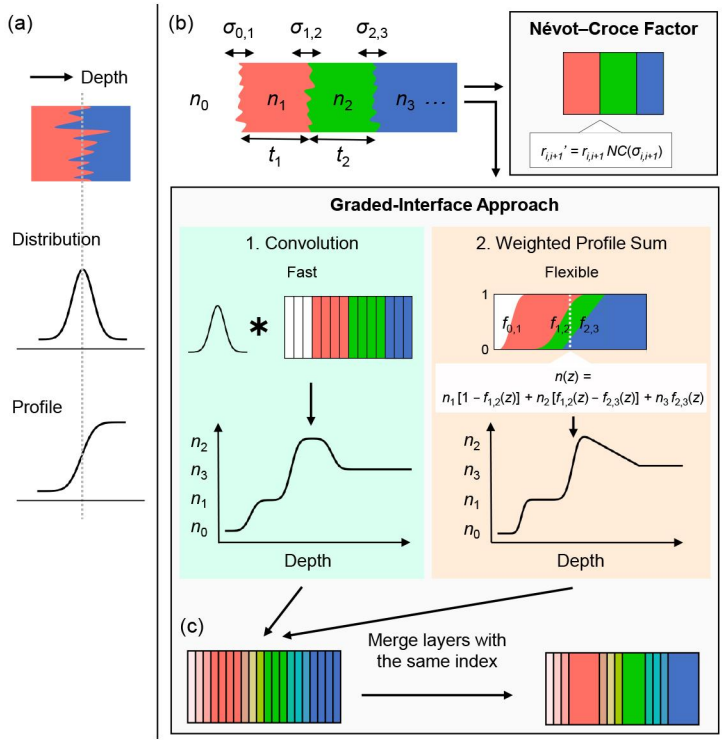

Fig. 1. Modeling roughness using the Névot–Croce factor and the graded-interface approach. (a) Roughness at an interface can be described by the distribution of the roughness and the profile that the refractive index transition takes as a function of depth. (b) Two approaches for taking account of roughness are discussed in this paper: the Névot–Croce factor approach and the graded-interface approach. Both approaches start with a model of the multilayer stack parametrized by layer thicknesses, refractive indices, and roughness. In the Névot–Croce factor approach, the Fresnel coefficient $r_{i,i+1}$ at each interface is corrected by the Névot–Croce factor NC, which is a function of the roughness at that interface, $\sigma_{i,i+1}$. For the graded-interface approach, we discuss two implementations. The first implementation is to convolve the distribution function with thinly discretized layers. The second implementation consists of creating a series of profiles corresponding to each interface, and then taking a weighted sum of the refractive indices. In both cases, the final model produced is a smooth profile of refractive index as a function of depth in the sample. (c) After a discretized stack is produced by one of the two implementations in (b), any layers with the same refractive index may be merged to improve computation speed in the subsequent Parratt formalism calculation.

The first and relatively simple implementation, illustrated on the left-hand side of Fig. 1(b), discretizes the stack of refractive indices into many thin layers, and then convolves the stack with a function that describes the distribution of all interfaces. This distribution function must sum to 1, and its characteristic width must correspond to the degree of roughness at all interfaces. While this implementation is easy to do, the obvious drawback is that it requires the model to have the same roughness width and shape at all the interfaces.

OSA CONTINUUM

The second implementation, illustrated on the right-hand side of Fig. 1(b), is to use the profile function at each of the interfaces. The derivative of a profile function is the distribution function that was used in the first approach. For example, for an interface with a Gaussian distribution function, its profile function takes the form of an error function. In this implementation, first, the profile function that transitions from 0 to 1 is prepared for each interface, with the correct profile shape. The functions must be centered in depth around the nominal location of the interface, and have characteristic widths corresponding to the degree of roughness. Then, the refractive index is calculated as the weighted sum of the refractive indices of the neighboring layers. Specifically, if an interface between the i^{th} and j^{th} layer is described by a function $f_{i,j}(z)$, then the effective refractive index $n(z)$ at depth z is calculated by:

$$n(z) = \sum_k r_k n_k \tag{3}$$

and

$$r_k = \begin{cases} 1 - f_{k,k+1} & k = 1 \\ f_{k-1,k} - f_{k,k+1} & 1<k<\text{end} \\ f_{k,k+1} & k = \text{end}, \end{cases}$$

where the summation is over the refractive indices of materials that are present at that z, and the index k runs from the index closest to the top surface. For example, if at a certain depth z, refractive indices n_1, n_2, and n_3 are present at that z, meaning two profile functions $f_{1,2}$ and $f_{2,3}$ are non-unity and non-zero as illustrated in Fig. 1(b), then $n(z) = n_1\left[1 - f_{1,2}(z)\right] + n_2\left[f_{1,2}(z) - f_{2,3}(z)\right] + n_3 f_{2,3}(z)$. While this implementation can be more time-consuming for a stack with a large number of interfaces, it is very versatile; it can handle different widths and profiles of roughness at each interface.

One advantage of using the graded-interface approach instead of the Névot–Croce factor is that it is more flexible, as illustrated in Fig. 2. By changing the distribution or profile function that represents the roughness, it is easy to model interfaces that do not have the typical normal distribution — some examples are shown in Fig. 2(a). The Névot–Croce factor as described by Eq. (1) is for normal distributions, and while there are other forms of the factor that correspond to different distributions [53], correction factors for distributions not covered by literature need to be newly derived. It is inadvisable to use the equation derived for normal distribution for modeling roughness with other distributions, since it has been shown that reflectance measurements are sensitive to the shape of the roughness distribution [10].

Another way in which the graded-interface approach is more flexible than using the Névot–Croce factor is in how it does not have to assume a uniform refractive index above and below the interface, as illustrated in Fig. 2(b). If there is some non-uniformity above/below the interface due to gradual change in density or dopant concentration, it is possible to represent that depth-dependent change as discretized layers, and to use the graded-interface approach to describe roughness between such layers, assuming that the depth-dependent change conforms to the shape of the interface.

Now, we describe four subtleties that need to be considered when using the graded-interface approach. The first is the overall extent of the distribution and profile functions used to model the interface. Some distribution functions, including the Gaussian distribution for a normally distributed roughness, theoretically have infinite extent, so in numerical modeling it is necessary to introduce some artificial cutoff to their range. We have found that we have good convergence when using Gaussians that extend from −3 to 3 standard deviations (i.e., using wider Gaussians only changed the result by a negligible amount), and we have used Gaussians truncated to this range for the simulations in this paper. However, it is preferable that a user tests how much the result changes for a given simulation for different extents of the used distribution function. Users

OSA CONTINUUM

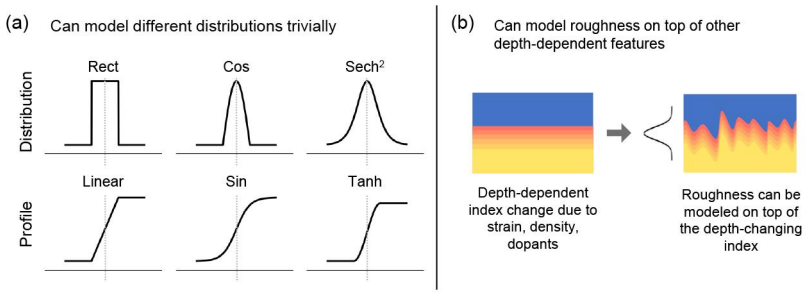

Fig. 2. Flexibility of the graded-interface approach. (a) The graded-interface approach allows easy modeling of arbitrary roughness distributions and profiles, for example rectangular, cosine and sech^2 distribution functions corresponding to linear, sine and tanh profile functions. (b) The graded-interface approach also allows modeling of roughness on top of other gradual, depth-dependent changes in the refractive index.

should also be careful to make sure that the sum of the distribution function is normalized to 1 after it is truncated.

The second consideration is the thickness into which the stacks are discretized. It is clearly preferable that a rough interface is described using many layers. As such, the discretization layer thickness should be considerably smaller than the smallest roughness in a given sample stack model. We have also found that the discretization thickness affects the phase shift upon reflection much more than the intensity reflectance because the discretization thickness changes the optical path length of incident light. Therefore, when simulating phase shift, it is preferable to use very finely discretized layers (which comes with an increased computational cost), and also test for the thickness at which simulation results begins to converge. As shown in Fig. 1(c), one way to combat the increase in computation time for a very finely discretized stack is to merge neighboring layers that share the same index so that the total number of layers, and thereby the number of computations, is reduced. The computation time for the Parratt formalism calculation is roughly linear in the number of interfaces.

It should be noted that, when solving for roughness in a physical sample using an iterative optimization method (such as the genetic algorithm) to fit experimental XRR or EUVR curves [54], it is only possible to solve for the parameters of interest with precision up to the discretization thickness. For continuous and very fine tuning of parameters, or for efficient computation time, the Névot–Croce factor is preferable.

The third subtlety is in calculating the phase shift upon reflection from a stack with roughness at the top interface. In the graded-interface approach, it is necessary to prepare discretized layers of whatever region the light approaches the sample from (usually vacuum, with refractive index of 1) at the top of the stack. This makes a smooth transition from the exterior region to the top material of the sample. When calculating the phase upon reflection from such a stack, however, the phase shift will be calculated at the top surface of the stack (with refractive index very close to that of the exterior region) and not from the nominal "top surface" at the center of the distribution that represents the top interface. Therefore, it is necessary to correct the calculated phase shift by subtracting the following factor φ from the calculated phase:

$$\varphi = 360^\circ\ [2h \sin(\theta)/\ \lambda], \tag{4}$$

where h is the height from the top surface of the modeled stack to the middle of the roughness distribution of the top interface, θ is the incidence angle measured from grazing, and λ is the wavelength of the light in the external medium. Note that different factors are needed for both the first and the last interface if calculating phase shift due to transmission.

OSA CONTINUUM

Lastly, when simulating roughness on a thin layer, users need to be careful not to have roughness at neighboring interfaces with a large difference. The reason for this is illustrated in Fig. 3. As shown in Fig. 3(a), using the graded-interface approach it is in fact possible to simulate layer thicknesses that are thinner than the total extent of the rough interface, provided that the thin layer conforms to the profile of the roughness it sits on. However, as shown in Fig. 3(b), if the roughness of neighboring interfaces differs too much with respect to the intermediate layer thickness, the lower layer will "penetrate" through the intermediate layer. If there are physical motivations to believe that this is the correct representation of the system being modeled, then it is possible to numerically represent such a system; however, it is not immediately compatible with the two implementations of the graded-interface approach discussed in this paper.

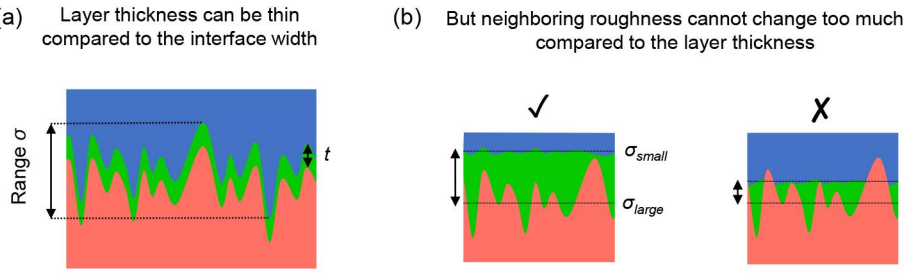

Fig. 3. Varying roughness on either side of a single, thin layer in the graded-interface approach. (a) It is possible to simulate layer thickness that is thinner than the range of the rough profile, as long as it is assumed that the layer conforms to the rough surface. (b) If the roughness of neighboring interfaces differs too much with respect to the intermediate layer thickness, one side of the layer will "penetrate" through.

Given these subtleties that come with the graded-interface approach, it may be that users should default to using the Névot–Croce factor, as long as the flexibility that comes with the graded-interface approach is unnecessary. However, this is only the case to the degree that calculations performed using the Névot–Croce factor and the graded-interface approach agree — otherwise, greater caution and investigation may be necessary to determine which approach should be used. The degree of agreement between the two approaches is the subject of the remainder of this paper.

5. Numerical simulations

5.1. Interpolation of scattering factors

Before comparing the Névot–Croce factor and the graded-interface approach using numerical simulations, it is important to consider to what accuracy we should scrutinize the two approaches. The answer is clearly experiment-dependent; it is not useful to try to chase down discrepancy in modeling that is many orders of magnitude smaller than the experimental error. In the following sections of the paper, by presenting results from a set of simulations, we will describe notable discrepancies in the results of the two approaches and highlight any aspects that users should consider when choosing between the two. We do not attempt to draw universal conclusions that are applicable to all XRR and EUVR experiments.

For all the following simulations, we used an in-house calculator based on the Parratt formalism, that has been tested extensively against IMD [22] for accuracy. Refractive indices of materials for the X-ray and EUV wavelengths were obtained using the following equation [55]:

$$n = 1 - \delta - i\beta = 1 - \frac{r_e}{2\pi}\lambda^2 \sum_i n_i(f_{1,i} + if_{2,i}), \tag{5}$$

OSA CONTINUUM

where n is the complex refractive index. In the X-ray and EUV regimes, the index is very close to 1 and so it is often expressed using δ, $\beta \ll 1$ (note that the sign on β can change depending on the convention used on the electromagnetic waves; $-i\beta$ is consistent with the plane wave representation of $\exp[i(\omega t - kr)]$, where ω is the radian frequency, and t and r are the temporal and spatial coordinates respectively). r_e is the classical electron radius, λ is the wavelength of the light in vacuum, n_i is the number of atoms of type i per unit volume, and $f_{1,i}$ and $f_{2,i}$ are the real and imaginary parts of the unitless atomic scattering factor for that atom type. Scattering factors are tabulated in multiple databases [56,57]; in this paper we use the database from Center for X-ray Optics (CXRO) [56]. We chose to use the CXRO database over Chantler's database [57], because while there is a good agreement between the CXRO's mostly experimental database and Chantler's theoretical database for energies above 1 keV, there is a large discrepancy for lower photon energies due to the ineffectiveness of the independent-particle approximation used in Chantler's calculation for lower photon energies.

In the CXRO tabulation, scattering factors are listed for discrete photon energies. Therefore, to calculate the refractive index of a material for an arbitrary photon energy/wavelength, it is necessary to interpolate the tabulated scattering factors. We have found that different interpolation methods cause slight differences in the final calculated reflectance. Here, we show the discrepancy in the interpolated refractive index and the complex reflectance between the modified Akima (makima) interpolation [58,59] and the piecewise cubic Hermite interpolating polynomial (pchip) [60,61], both available in MATLAB's interp1 function. We show this for bulk Si (shown in Fig. 4), Cu, Al, and Au (shown in the appendix Fig. 12). For each element, we selected two wavelengths, one that is far from a transition edge (i.e., scattering factor vs. wavelength curve is smooth) and near an edge (i.e., scattering factor changes sharply), and in particular we selected wavelengths that are in between the tabulated CXRO datapoints. We found that far from transition edges, the calculated intensity reflectance can vary on orders of 1E−6% to 1E−3% of the mean reflectance, and the phase shift upon reflection can vary on orders of (1E−7)° to (1E−4)° depending on the incidence angle. However, when interpolating near transition edges, the intensity reflectance varied by up to 1 to 10% of the mean, and phase shift by up to 1°. The pchip and makima interpolations were chosen for this demonstration for their relatively good agreement with each other, and it should be noted that other lower-order interpolation schemes (linear, next, previous, spline) resulted in considerably larger discrepancies. Therefore, even when assuming that the tabulated scattering factors are errorless (which is certainly not true, but this error is often not accounted for in data analysis), simulated reflectance should be taken with some caution, especially when calculated very close to transition edges.

5.2. Summary of simulation parameters

Here we report on the parameters and settings used in our simulations. When using the Névot–Croce factor, the form assuming a normal distribution of roughness given by Eq. (1) was used. For the graded-interface approach, we used the weighted profile sum implementation and used error functions as the profile at all interfaces. The range of the error functions was limited so that it represents the integral of a Gaussian function that is truncated at −3 and 3 standard deviations. The discretization thickness was set at 0.0005 nm (which is finer than is typically needed), and before passing the stack to a Parratt formalism calculator we combined any adjacent layers with the same refractive index for increased computational speed. The piecewise-cubic Hermite interpolating polynomial (pchip) scheme was used to interpolate the scattering factors for calculating the refractive index. We assumed that in each case the light was incident from vacuum.

OSA CONTINUUM

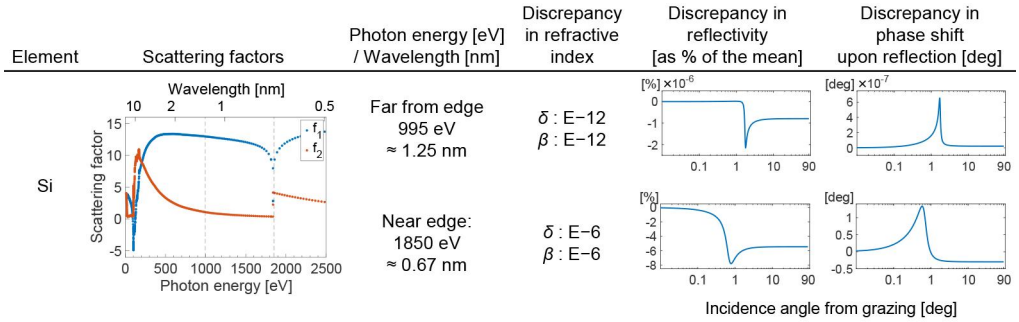

Fig. 4. Discrepancy in calculated complex reflectance from bulk elements (with no surface roughness) between using the modified Akima (makima) and piecewise-cubic Hermite interpolating polynomial (pchip) schemes to interpolate scattering factors, which are needed to calculate the complex refractive index. The scattering factor was interpolated at two photon energies far from and close to a transition edge, as indicated by the dotted lines in the scattering factors plot. At each photon energy, the order of magnitude of discrepancy in the interpolated refractive index is given, and the discrepancy in the amplitude and the phase shift upon reflection for S-polarization is plotted as a function of incidence angle from grazing.

5.3. *Reflectance from a rough bare substrate*

Here we compare X-ray and EUV reflectance from bulk Si with a rough surface, where the RMS roughness was scanned between 0 and 5 nm in 0.5 nm increments. This is shown in Fig. 5 for S-polarization, and the corresponding figure for P-polarization is shown in the appendix Fig. 13. The density of Si was set to 2.329g/cm^3, with the resulting refractive index calculated using Eq. (5) for 0.154 nm ≈ 8.04 keV (typical wavelength for XRR, Cu K-α) being $1 - 7.58\text{E}{-6} - 1.72\text{E}{-7}i$, and for 13.5 nm ≈ 91.8eV (wavelength for EUV lithography) being $1 - 1.02\text{E}{-3} - 1.83\text{E}{-3}i$. The plots in Fig. 5 show only the regions with reflectance of above 1E−8, since lower reflectance is often not recorded with enough signal-to-noise ratio, and also because the graded-interface approach had oscillations in the curves that are most likely due to numerical artifacts.

The first row of Fig. 5 shows the intensity reflectance and the phase shift upon reflection calculated using the Névot–Croce factor. The second row shows how the curves calculated using the Névot–Croce factor deviate from those simulated for a perfect interface. Intensity reflectance is shown as a ratio $|R/R_0|$, where $R = |r|^2$ is the intensity reflectance calculated from a rough surface, and $R_0 = |r_0|^2$ is the intensity reflectance calculated from a perfectly smooth surface, and r and r_0 are the corresponding complex field reflectance. Phase is shown as angle(r/r_0). The third row is the difference in $|R/R_0|$ and angle(r/r_0) calculated using the Névot–Croce factor and the graded-interface approach. If values of the curves in the third row are large, then the Névot–Croce and the graded-interface approach differ significantly in their prediction of how roughness affects complex reflectance.

In general, the difference between the reflectance calculated by the Névot–Croce and graded-interface approach is more significant for X-ray wavelengths, which is expected since the probed roughness is large compared to the wavelength. Even for X-rays, the discrepancy in intensity reflectance is relatively small, especially for low roughness. However, the discrepancy in phase is quite significant; even for a modest RMS roughness of 1 nm, the discrepancy reaches 5°. This is the aforementioned discrepancy in phase between the Névot–Croce factor and the graded-interface approach. Hamilton and Pynn argue that the discrepancy does not reflect actual physics but is a shortcoming of the approximation made in deriving the Névot–Croce factor [35]; however, this

OSA CONTINUUM

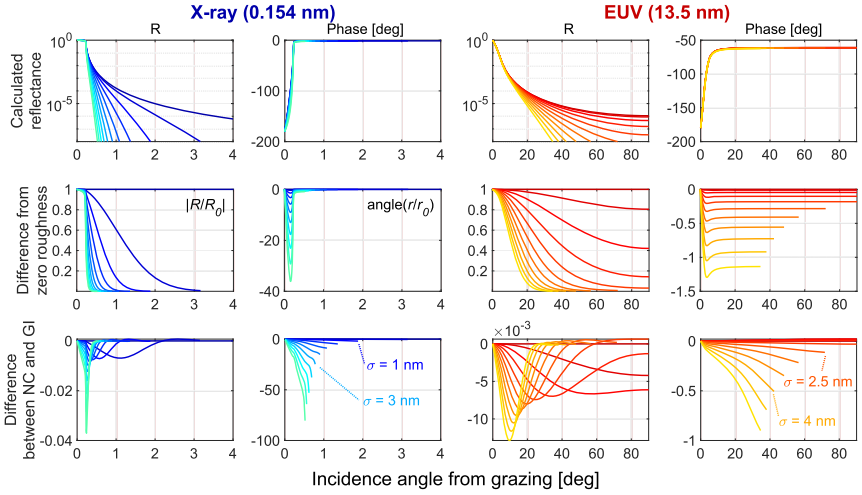

Fig. 5. Difference in calculated reflectance from bulk Si with varying surface roughness. Shown for X-ray wavelength of 0.154 nm (blue curves, first two columns) and EUV wavelength of 13.5 nm (red curves, last two columns). The darker colors correspond to smaller roughness, where the roughness was scanned between 0 and 5 nm in 0.5 nm increments. For each wavelength, the left column shows the intensity reflectance R, while the right column shows the phase upon reflection. **Top row**: calculated complex reflectance using the Névot–Croce factor. **Middle row**: deviation from perfectly smooth surface, calculated using the Névot–Croce factor; intensity reflectance is shown as a ratio $|R/R_0|$, where $R = |r|^2$ is the intensity reflectance calculated from a rough surface, and $R_0 = |r_0|^2$ is the intensity reflectance calculated from a perfectly smooth surface, and r and r_0 are the corresponding complex field reflectance. Phase is shown as angle(r/r_0). **Bottom row**: $|R/R_0|$ and angle(r/r_0) from Névot–Croce factor (NC) minus those of the graded-interface approach (GI). For all plots, only the parts of the plot with intensity reflectance above 1E−8 are shown.

point should be further investigated if one wishes to use the Névot–Croce factor for accurate prediction of the phase shift of reflected X-rays.

Unsurprisingly, the discrepancy is smaller for EUV wavelengths, even for near-normal incidence angles. Below an RMS roughness of 1.5 nm, the discrepancy is below 0.007 in $|R/R_0|$ and 0.04° in angle(r/r_0). The numbers are similar for P-polarization as well, although the discrepancy increases around the Brewster angle. It should also be noted that at a wavelength of 10.8 nm, where refractive index of Si deviates relatively far from unity, the discrepancy for 1.5 nm roughness did increase to around 0.01 in $|R/R_0|$ and 0.2° in in angle(r/r_0). This is most likely because the Névot–Croce factor is derived under the assumption that there is only a small difference in the refractive index of the media separated by the interface.

5.4. *Reflectance from a monolayer*

Next, we compare X-ray and EUV reflectance from a monolayer where both the vacuum–monolayer and the monolayer–substrate interfaces have roughness.

We compare X-ray and EUV reflectance from a monolayer of SiO_2 on a bulk Si substrate. We assume that the surface roughness at both the vacuum–SiO_2 interface and the SiO_2–Si interface has RMS roughness of 1 nm, and we vary the thickness of the SiO_2 monolayer between 10–1 nm in increments of 1 nm. This is shown in Fig. 6 for S-polarization, and the corresponding figure for P-polarization is shown in the appendix Fig. 14. The density of Si and the resulting refractive

OSA CONTINUUM

index are as quoted in Sec. 5.3, and the density of SiO_2 was set to 2.196g/cm^3 (assuming amorphous), with resulting refractive index of $1 - 7.11\text{E}{-6} - 9.18\text{E}{-8}i$ for the X-ray wavelength, and $1{-}2.20\text{E}{-2} - 1.08\text{E}{-2}i$ for the EUV wavelength.

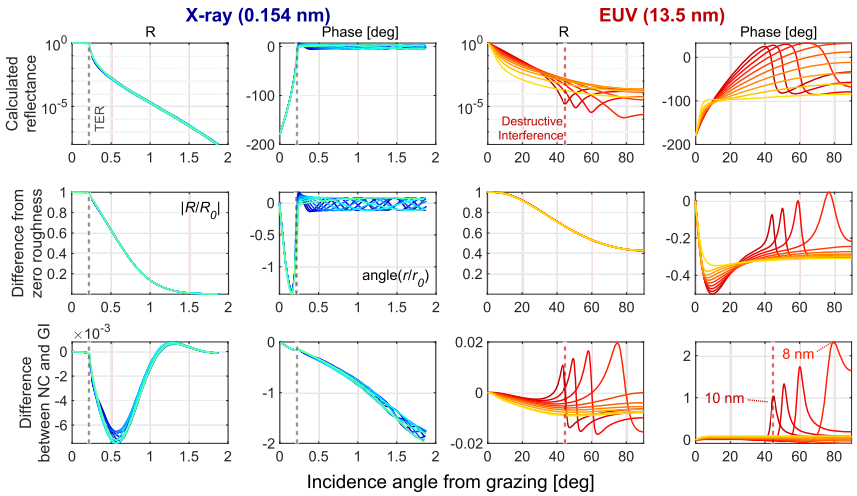

Fig. 6. Difference in calculated reflectance from a SiO_2 monolayer on Si substrate with varying monolayer thickness shown for X-ray wavelength of 0.154 nm (blue curves, first two columns) and EUV wavelength of 13.5 nm (red curves, last two columns). The darker colors correspond to larger thickness, where the thickness was scanned between 10 and 1 nm in 1 nm increments. The roughness at both interfaces was set to 1 nm. The gray dotted vertical lines in the X-ray plots correspond to the threshold of total external reflection (TER), while the red dotted vertical lines in the EUV plots correspond to the destructive interference angle for the monolayer thickness of 10 nm.

Notably, the discrepancy between the Névot–Croce factor and the graded-interface approach peaks at around the angle where the intensity reflectance drops due to destructive interference from the monolayer. For the X-ray wavelength, there are numerous interference fringes at many angles past the total external reflection angle for all the tested layer thicknesses, and so the discrepancy between the Névot–Croce factor and the graded-interface approach as a function of incidence angle does not differ too much between the different monolayer thicknesses. However, for the EUV wavelength, oscillations in intensity reflectance are observable for larger monolayer thicknesses, and the discrepancy clearly peaks at these positions. The same behavior is observed for P-polarization as well, at both the destructive interference angles and the Brewster's angle.

To visualize this behavior more clearly, we plot the discrepancy between the two methods in intensity reflectance and phase shift upon reflection as a function of both wavelength and incidence angle, for roughness of 0.1 nm at both interfaces, and fixed monolayer thickness of 5 nm. In this simulation, the refractive indices of SiO_2 and Si were kept constant at the value corresponding to wavelength of 12 nm to observe the phenomena without the influence of changing refractive index as a function of wavelength. This is shown in Fig. 7. As can be seen, the discrepancy in intensity reflectance peaks in two places, before and after the minima of intensity reflectance (shown as an overlaid contour lines), corresponding to destructive interference. The discrepancy in phase shift upon reflection peaks right at the minima of intensity reflectance.

5.5. *Reflectance from multilayer mirrors*

It was observed in the previous section that the discrepancy between the Névot–Croce factor and the graded-interface approach is high around minima of intensity reflectance. This poses the

OSA CONTINUUM

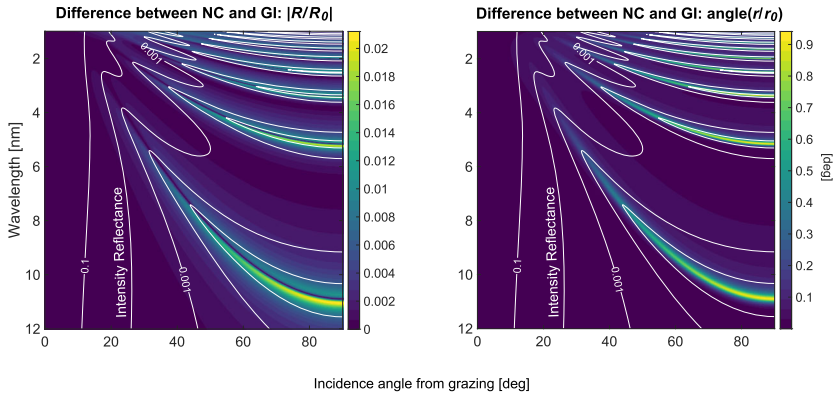

Fig. 7. Absolute difference in reflectance calculated using the Névot–Croce factor (NC) and the graded-interface approach (GI), shown as a function of incidence angle and wavelength for S-polarization, for a SiO_2 monolayer on Si. Difference in the intensity reflectance is shown as a difference in the ratio $|R/R_0|$, where $R = |r|^2$ is the intensity reflectance calculated from a rough surface, and $R_0 = |r_0|^2$ is the intensity reflectance calculated from a perfectly smooth surface, and r and r_0 are the corresponding complex field reflectance. Phase is shown as difference in angle(r/r_0). The overlaid contour lines correspond to the intensity reflectance calculated using the Névot–Croce factor.

question of how the discrepancy behaves from multilayer optics that consist of many thin layers and utilize constructive/destructive interference to obtain a desired reflectance curve.

We compare X-ray and EUV complex reflectance from multilayer mirrors designed for the two respective wavelengths. For X-ray wavelength of 0.154 nm, we simulate a W/C multilayer mirror [62], consisting of 20 pairs of W/C layers, with W thickness of 1 nm and C thickness of 3.3 nm, on a Si substrate. The refractive index of Si is the same as in Sec. 5.3, and the density of W and C are set to 16.0 and 2.0 g/cm^3 with resulting refractive indices 1–3.85E−5–3.22E−6i and 1–6.42E−6–1.02E−8i respectively.

For an EUV wavelength of 13.5 nm, we model a Mo/Si multilayer mirror with 30 pairs, with Mo thickness of 3.38 nm and Si thickness of 6.27 nm, on a SiO_2 substrate. The refractive index of Si and SiO_2 are as listed in Sec. 5.3–4, and the density of Mo is set to 10.28 g/cm^3 with resulting refractive index of 1–7.67E−2–6.48E−3i. The roughness at all interfaces in both the X-ray and EUV multilayer mirrors was set to 0.3 nm.

Figure 8 shows the simulated reflectance from the multilayer mirrors and the discrepancy between the two approaches for S-polarization. Notably, the discrepancy at the reflectance peak (marked with a green circle) is relatively low, especially considering that there are many interfaces in the stack. At the reflectance peak, for X-ray the discrepancy in $|R/R_0|$ is 0.002 and for angle(r/r_0) it is 0.09°. For EUV, they are 0.0003 and 0.3° respectively.

However, away from the reflectance peak and in the Kiessig fringes, the discrepancy between the two methods fluctuates significantly. From the insets of Fig. 8, it can be seen that the discrepancy in intensity reflectance peaks in opposite directions on two sides of the intensity minima (as was also seen in Fig. 6 and 7), and the discrepancy in phase peaks both at the intensity maxima and the minima. One plausible explanation for this is that the Névot–Croce factor does deviate from known theoretical solutions as well as the graded-interface approach in simulating phase shift upon reflection. While this is not important for intensity measurements from bulk materials, it does manifest in both the simulated intensity and phase shift upon reflection from layered materials because the phase upon reflection from each interface will couple into the overall reflectance through interference. To our knowledge this point has not been discussed in

OSA CONTINUUM

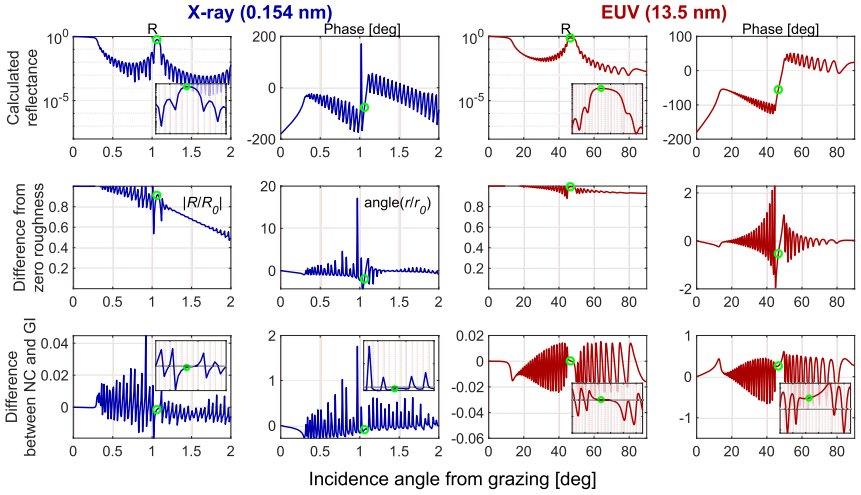

Fig. 8. Difference in the calculated reflectance from multilayer mirrors, for an X-ray wavelength of 0.154 nm (blue curve, first two columns) and an EUV wavelength of 13.5 nm (red curve, last two columns). The angle of maximum reflectance is circled in green in each of the plots. Insets show a zoom-in around the angle of maximum reflectance, where the range in incidence angle is 0.25 deg for the X-ray insets and 5 deg for the EUV insets.

previous literature, but it should be a consideration when using the Névot–Croce factor in XRR or EUVR to solve for interface quality, since these techniques rely heavily on interference fringes in the data analysis.

We also look at angle and wavelength selectivity of multilayer mirrors, which are parameters of interest especially when these mirrors are being used for wavelength selection. Figure 9 shows the difference in the maximum reflectance, the angle at which it happens, and FWHM range in the incidence angle and the wavelength. We see that the discrepancies are very small.

X-ray	Max. reflectance	Angle of max. reflectance [deg from grazing]	FWHM range in incidence angle [deg]	FWHM range in wavelength [nm]
Névot–Croce	0.5879	1.0636	0.0611	0.00880
Graded Interface	0.5888	1.0636	0.0612	0.00881
Difference	**0.0009**	**<0.0001**	**0.0001**	**0.00001**

EUV	Max. reflectance	Angle of max. reflectance [deg from grazing]	FWHM range in incidence angle [deg]	FWHM range in wavelength [nm]
Névot–Croce	0.7532	46.50	4.99	0.964
Graded Interface	0.7530	46.51	5.00	0.964
Difference	**0.0002**	**0.01**	**0.01**	**<0.001**

Fig. 9. Discrepancies in the angle of maximum reflectance, and angle and wavelength selectivity for X-ray (top) and EUV (bottom) multilayer mirror. The discrepancies are small.

Finally, we test whether the discrepancy between the Névot–Croce factor and the graded-interface approach grows for increasing number of multilayer pairs. Figure 10 shows how the discrepancy between the two approaches changes for increasing number of multilayer pairs, using

OSA CONTINUUM

the previously mentioned multilayer mirror designs. The incidence angle was set to that of the maximum-intensity reflectance (1.0636° for X-ray and 46.5° for EUV). While the discrepancy in phase shift upon reflection generally grows as a function of number of multilayer pairs (and then plateaus), that is not the case for the intensity reflectance.

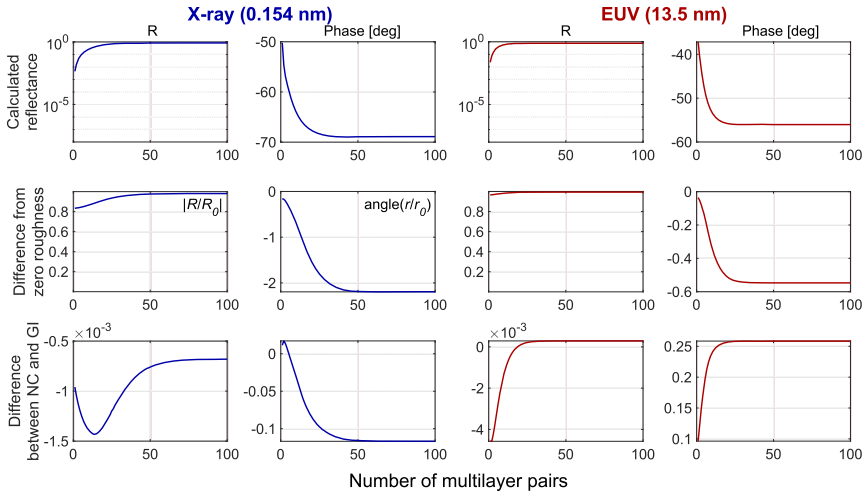

Fig. 10. Difference in calculated reflectance from multilayer mirrors, as a function of number of multilayer pairs. See main text for the multilayer mirror designs. Shown for X-ray wavelength of 0.154 nm (blue curve, first two columns) and EUV wavelength of 13.5 nm (red curve, last two columns). The incidence angle was set to that of the maximum-intensity reflectance.

6. Conclusion

The Névot–Croce factor and the graded-interface approach are two approaches for modeling surface and interface roughness in a transversely uniform system when simulating X-ray and EUV reflectance. The Névot–Croce factor is simple to implement and is computationally fast. The graded-interface approach is more flexible and can trivially accommodate different roughness profiles and other depth-dependent features.

When choosing between the two methods, it is important to verify that the two methods produce similar results. We have found that, while the discrepancy between the two methods is small for most cases, it can be large in several notable cases: when the roughness is large with respect to the wavelength (especially in simulating the phase shift upon reflection), when refractive index changes significantly across the interface, at angles corresponding to high constructive and destructive interference (the extrema of Kiessig fringes), at Brewster's angle for P-polarization, and away from the designed bandwidth of multilayer mirrors. While the first two cases are widely known, we emphasize an important subtlety in that the two approaches deviate from each other in simulating the phase upon reflection, and that the error is coupled into intensity reflectance when there are multiple interfaces in the system being modeled. To our knowledge, this is the first time the latter point has been discussed. Additionally, the last point on multilayer mirrors is important for characterizing multilayer mirrors using XRR or EUVR, where one may measure outside of the design bandwidth to determine mirror characteristics. These conclusions are summarized in Fig. 11.

OSA CONTINUUM

Névot–Croce	Graded Interface
Simple to implement Computationally **fast**	**Flexible** — can accommodate different profiles, other depth-dependent features

Results sensitive to modeling approach…

- For larger σ with respect to λ, especially in phase shift upon reflection
- When refractive index changes significantly across the interface
- Around interference peaks and troughs
- At Brewster's angle for P-polarization

Fig. 11. Summary of differences between the Névot–Croce factor and the graded-interface approach, and where the discrepancy between the two approaches is large.

Appendix

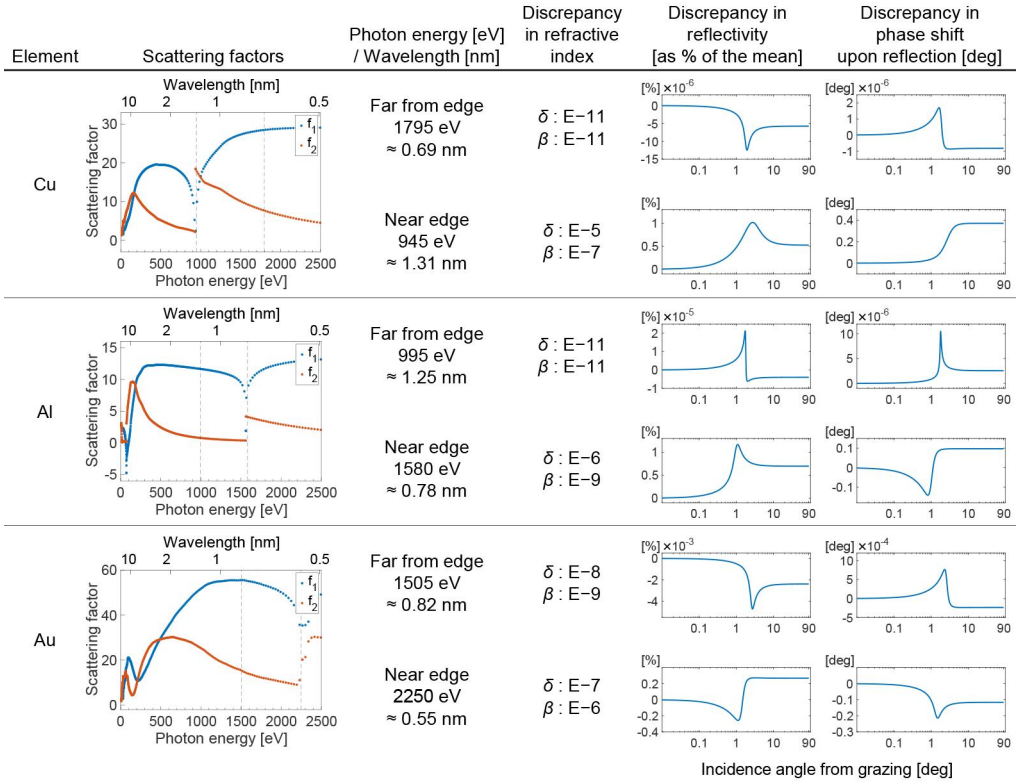

Fig. 12. Extension of Fig. 4, discrepancy in calculated complex reflectance and from bulk elements (with no surface roughness) between using the modified Akima (makima) and piecewise cubic Hermite interpolating polynomial (pchip) schemes to interpolate scattering factors, shown for more elements.

OSA CONTINUUM

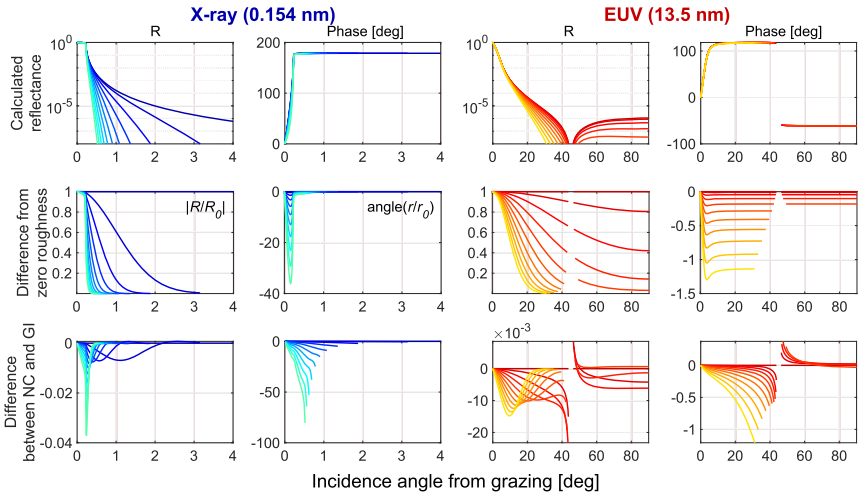

Fig. 13. P-polarization version of Fig. 5 (reflectance from a bare Si substrate for varying roughness).

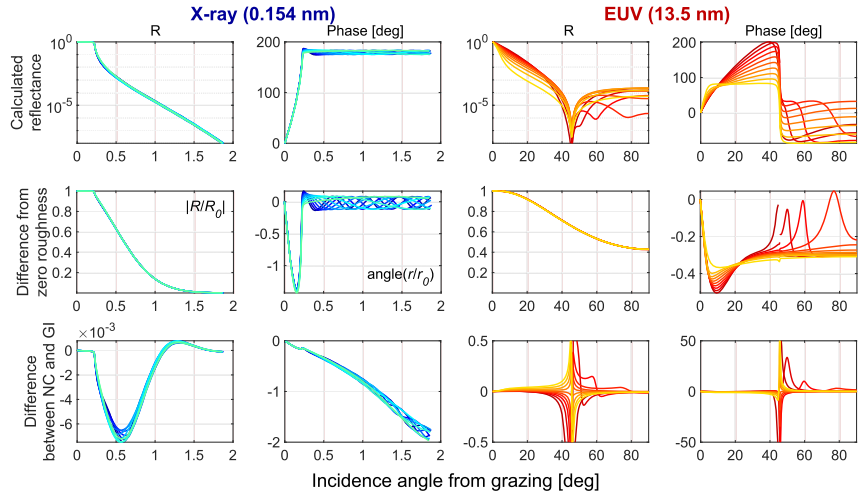

Fig. 14. P-polarization version of Fig. 6 (reflectance from SiO_2 monolayer on Si substrate for varying monolayer thickness). The y-axis of the bottom row plots for the EUV wavelength has been zoomed-in for visibility.

OSA CONTINUUM

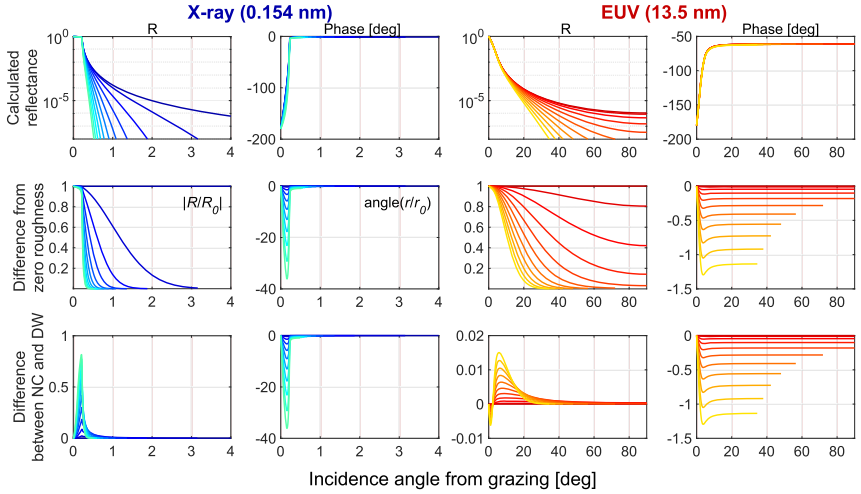

Fig. 15. Difference in the results of the Névot–Croce (NC) and the Debye–Waller (DW) factor for calculating reflectance off of bulk Si (same setup as Fig. 5 and Fig. 13). The first and the second rows are shown for the Névot–Croce factor, and the third row shows the difference between the Névot–Croce and the Debye–Waller factor. The plots are shown for S-polarization, and the roughness was scanned between 0 and 5 nm in 0.5 nm increments. Note that in this case, the Debye–Waller factor is purely real, so the difference between the Névot–Croce and the Debye–Waller in phase is purely the phase in the Névot–Croce factor.

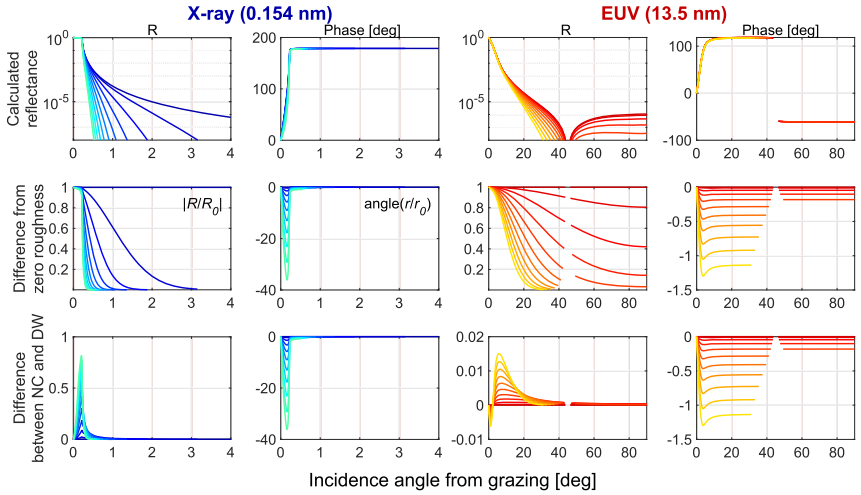

Fig. 16. P-polarization version of Fig. 15 (difference in the Névot–Croce and the Debye–Waller factor for calculating reflectance off of bulk Si).

OSA CONTINUUM

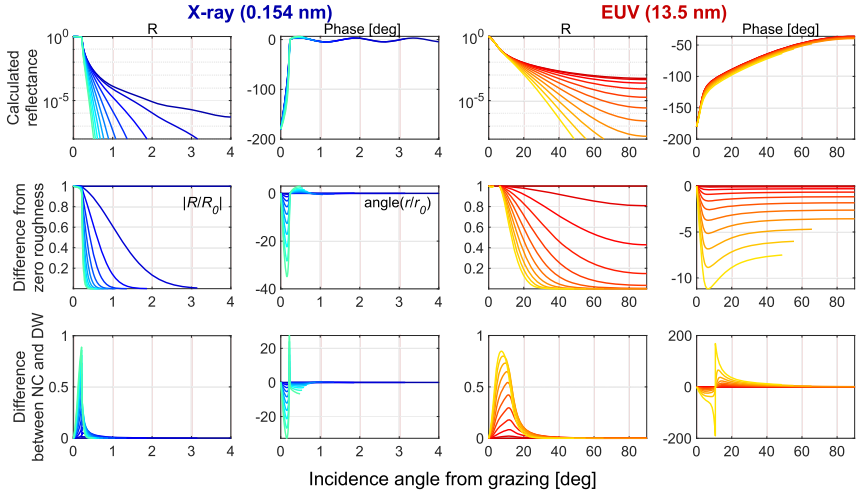

Fig. 17. Difference in the results of the Névot–Croce (NC) and the Debye–Waller (DW) factor for calculating reflectance off of 3 nm of SiO_2 monolayer on Si (similar setup as Fig. 6 and Fig. 14). The first and the second rows are shown for the Névot–Croce factor, and the third row shows the difference between the Névot–Croce and the Debye–Waller factor. The plots are shown for S-polarization, and the roughness was scanned between 0 and 5 nm in 0.5 nm increments.

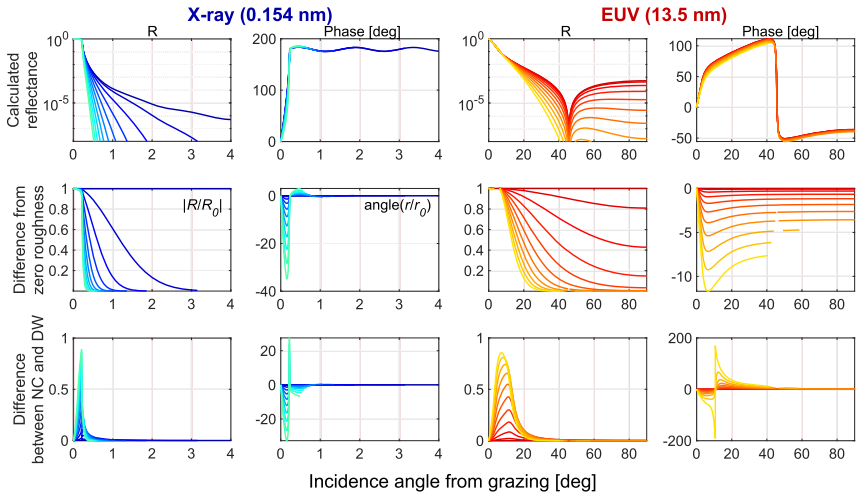

Fig. 18. P-polarization version of Fig. 17 (difference in the Névot–Croce and the Debye–Waller factor for calculating reflectance off of SiO_2 monolayer on Si).

Funding. National Science Foundation (STROBE STC DMR-1548924); U.S. Department of Defense (140D0419C0094, DARPA W31P4Q-17-C-0104); China Scholarship Council (201806260040).

Disclosures. H.K.: KMLabs Inc. (I, E, P). M.M.: KMLabs Inc. (I, P). Other authors declare no conflicts of interest.

Data availability. Data underlying the results presented in this paper are not publicly available at this time but may be obtained from the authors upon reasonable request.

OSA CONTINUUM

References

1. A. Martinez, N. Seoane, A. R. Brown, J. R. Barker, and A. Asenov, "Variability in Si Nanowire MOSFETs Due to the Combined Effect of Interface Roughness and Random Dopants: A Fully Three-Dimensional NEGF Simulation Study," IEEE Trans. Electron Devices **57**(7), 1626–1635 (2010).
2. K. Mori, S. Samata, N. Mitsugi, A. Teramoto, R. Kuroda, T. Suwa, K. Hashimoto, and S. Sugawa, "Influence of silicon wafer surface roughness on semiconductor device characteristics," Jpn. J. Appl. Phys. **59**(SM), SMMB06 (2020).
3. Y. Arisawa, T. Terasawa, and H. Watanabe, "Impact of EUV mask roughness on lithography performance," Proc. SPIE **8679**, 86792S (2013).
4. K. Rook, P. Turner, N. Srinivasan, T. Henry, K. Yamamoto, and M. Lee, "Process optimization for performance improvement in Mo/Si multilayers for EUV mask blanks," Proc. SPIE **11517**, 1151708 (2020).
5. H. Sakaki, T. Noda, K. Hirakawa, M. Tanaka, and T. Matsusue, "Interface roughness scattering in GaAs/AlAb quantum wells," Appl. Phys. Lett. **51**(23), 1934–1936 (1987).
6. J. Kudrnovský, V. Drchal, I. Turek, M. Šob, and P. Weinberger, "Interlayer magnetic coupling: Effect of interface roughness," Phys. Rev. B **53**(9), 5125–5128 (1996).
7. A. Paul, "Effect of interface roughness on magnetic multilayers of Fe/Tb and Fe/Cr," J. Magn. Magn. Mater. **240**(1-3), 497–500 (2002).
8. C. Liu, C. Yu, H. Jiang, L. Shen, C. Alexander, and G. J. Mankey, "Effect of interface roughness on the exchange bias for NiFe/FeMn," J. Appl. Phys. **87**(9), 6644–6646 (2000).
9. E. Chason and T. Mayer, "Thin film and surface characterization by specular X-ray reflectivity," Critical Reviews in Solid State and Materials Sciences **22**(1), 1–67(1997).
10. K. N. Stoev and K. Sakurai, "Review on grazing incidence X-ray spectrometry and reflectometry," Spectrochim. Acta, Part B **54**(1), 41–82 (1999).
11. E. M. Gullikson, J. H. Underwood, P. C. Batson, and V. Nikitin, "A soft x-ray/EUV reflectometer based on a laser produced plasma source," J. X-Ray Sci. Technol. **3**(4), 283–299 (1992).
12. F. Scholze, J. Tümmler, and G. Ulm, "High-accuracy radiometry in the EUV range at the PTB soft x-ray beamline," Metrologia **40**(1), S224–S228 (2003).
13. C. Tarrio, S. Grantham, M. B. Squires, R. E. Vest, and T. B. Lucatorto, "Towards High Accuracy Reflectometry for Extreme-Ultraviolet Lithography," J. Res. Natl. Inst. Stand. Technol. **108**(4), 267–273 (2003).
14. S. Döring, F. Hertlein, A. Bayer, and K. Mann, "EUV reflectometry for thickness and density determination of thin film coatings," Appl. Phys. A **107**(4), 795–800 (2012).
15. S. Danylyuk, S. Herbert, P. Loosen, R. Lebert, A. Schäfer, J. Schubert, M. Tryus, and L. Juschkin, "Multi-angle spectroscopic extreme ultraviolet reflectometry for analysis of thin films and interfaces," Phys. Status Solidi **12**(3), 318–322 (2015).
16. M. G. Sertsu, M. Nardello, A. Giglia, A. J. Corso, C. Maurizio, L. Juschkin, and P. Nicolosi, "Analysis of buried interfaces in multilayer mirrors using grazing incidence extreme ultraviolet reflectometry near resonance edges," Appl. Opt. **54**(35), 10351–10358 (2015).
17. H. Iguchi, H. Hashimoto, M. Kuki, T. Harada, H. Kinoshita, T. Watanabe, Y. Y. Platonov, M. D. Kriese, and J. R. Rodriguez, "Extreme-ultraviolet collector mirror measurement using large reflectometer at NewSUBARU synchrotron facility," Jpn. J. Appl. Phys. **55**(6S1), 06GC01 (2016).
18. F. Hertlein, A. Oehr, C. Hoffmann, C. Michaelsen, and J. Wiesmann, "State-of-the-art of multilayer optics for laboratory X-ray devices," Part. Part. Syst. Charact. **22**(6), 378–383 (2005).
19. G. A. Valkovskiy, M. V. Baidakova, P. N. Brunkov, S. G. Konnikov, M. A. Yagovkina, and J. M. Zadiranov, "Study of roughness in multilayer Mo-Si mirrors," Phys. Status Solidi A **208**(11), 2623–2628 (2011).
20. Y. Liu, Q. Huang, R. Qi, L. Xiao, Z. Zhang, and Z. Wang, "Improvement of the Microstructure and X-ray Performance of Ultrathin Ru/C Multilayer Mirror after High Temperature Treatment," Coatings **11**(1), 45 (2021).
21. L. G. Parratt, "Surface Studies of Solids by Total Reflection of X-Rays," Phys. Rev. **95**(2), 359–369 (1954).
22. D. L. Windt, "IMD—Software for modeling the optical properties of multilayer films," Comput. Phys. **12**(4), 360–370 (1998).
23. M. Born and E. Wolf, "Wave propagation in a stratified medium. Theory of dielectric films," in *Principles of Optics* (2001), pp. 54–74.
24. L. Névot and P. Croce, "Caractérisation des surfaces par réflexion rasante de rayons X. Application à l'étude du polissage de quelques verres silicates," Rev. Phys. Appl. **15**(3), 761–779 (1980).
25. L. Nevot, B. Pardo, and J. Corno, "Characterization of X-UV multilayers by grazing incidence X-ray reflectometry," Rev. Phys. Appl. **23**(10), 1675–1686 (1988).
26. E. M. Gullikson, "Optical Properties of Materials," in *Experimental Methods in the Physical Sciences* (Academic Press, 1998), Vol. 31, pp. 257–270.
27. D. K. G. de Boer, "X-ray scattering and x-ray fluorescence from materials with rough interfaces," Phys. Rev. B **53**(10), 6048–6064 (1996).
28. R. A. Bartels, A. Paul, H. Green, H. C. Kapteyn, M. M. Murnane, S. Backus, I. P. Christov, Y. Liu, D. Attwood, and C. Jacobsen, "Generation of Spatially Coherent Light at Extreme Ultraviolet Wavelengths," Science **297**(5580), 376–378 (2002).

OSA CONTINUUM

29. A. Rundquist, C. G. Durfee III, Z. Chang, C. Herne, S. Backus, M. M. Murnane, and H. C. Kapteyn, "Phase-Matched Generation of Coherent Soft X-rays," Science **280**(5368), 1412–1415 (1998).
30. E. R. Shanblatt, C. L. Porter, D. F. Gardner, G. F. Mancini, R. M. Karl, M. D. Tanksalvala, C. S. Bevis, V. H. Vartanian, H. C. Kapteyn, D. E. Adams, and M. M. Murnane, "Quantitative Chemically Specific Coherent Diffractive Imaging of Reactions at Buried Interfaces with Few Nanometer Precision," Nano Lett. **16**(9), 5444–5450 (2016).
31. T. Harada, H. Hashimoto, T. Amano, H. Kinoshita, and T. Watanabe, "Phase imaging results of phase defect using micro-coherent extreme ultraviolet scatterometry microscope," J. Micro/Nanolith. MEMS MOEMS **15**(2), 021007 (2016).
32. C. Zhu, R. Harder, A. Diaz, V. Komanicky, A. Barbour, R. Xu, X. Huang, Y. Liu, M. S. Pierce, A. Menzel, and H. You, "Ptychographic x-ray imaging of surfaces on crystal truncation rod," Appl. Phys. Lett. **106**(10), 101604 (2015).
33. M. Tanksalvala, C. L. Porter, Y. Esashi, B. Wang, N. W. Jenkins, Z. Zhang, G. P. Miley, J. L. Knobloch, B. McBennett, N. Horiguchi, S. Yazdi, J. Zhou, M. N. Jacobs, C. S. Bevis, R. M. Karl Jr, P. Johnsen, D. Ren, L. Waller, D. E. Adams, S. L. Cousin, C. Liao, J. Miao, M. Gerrity, H. C. Kapteyn, and M. M. Murnane, "Nondestructive, high-resolution, chemically specific 3D nanostructure characterization using phase-sensitive EUV imaging reflectometry," Sci. Adv. **7**(5), eabd9667 (2021).
34. S. Sherwin, I. Cordova, L. Waller, A. Neureuther, and P. Naulleau, "Measuring the Phase of EUV Photomasks," Proc. SPIE **11147**, 11147F (2019).
35. W. A. Hamilton and R. Pynn, "The effect of surface roughness on the phase of neutrons specularly reflected at grazing incidence," Phys. B **173**(1-2), 71–73 (1991).
36. A. Caticha, "Reflection and transmission of x rays by graded interfaces," Phys. Rev. B **52**(13), 9214–9223 (1995).
37. J. Lekner, "Exact results," in *Theory of Reflection of Electromagnetic and Particle Waves* (Springer, 1987), pp. 33–60.
38. B. B. Luokkala, S. Garoff, and R. M. Suter, "Using x-ray reflectivity to determine the structure of surfactant monolayers," Phys. Rev. E **62**(2), 2405–2415 (2000).
39. D. K. G. de Boer and A. J. G. Leenaers, "Probing interface roughness by X-ray scattering," Phys. B **221**(1-4), 18–26 (1996).
40. D. Bahr, W. Press, R. Jebasinski, and S. Mantl, "X-ray reflectivity and diffuse-scattering study of CoSi2 layers in Si produced by ion-beam synthesis," Phys. Rev. B **47**(8), 4385–4393 (1993).
41. R. Pynn, "Neutron scattering by rough surfaces at grazing incidence,"Phys. Rev. B **45**(2), 602–612 (1992).
42. C. Teichert, J. F. MacKay, D. E. Savage, M. G. Lagally, M. Brohl, and P. Wagner, "Comparison of surface roughness of polished silicon wafers measured by light scattering topography, soft-x-ray scattering, and atomic-force microscopy," Appl. Phys. Lett. **66**(18), 2346–2348 (1995).
43. J. M. Elson, J. P. Rahn, and J. M. Bennett, "Relationship of the total integrated scattering from multilayer-coated optics to angle of incidence, polarization, correlation length, and roughness cross-correlation properties," Appl. Opt. **22**(20), 3207–3219 (1983).
44. S. K. Sinha, E. B. Sirota, S. Garoff, and H. B. Stanley, "X-ray and neutron scattering from rough surfaces," Phys. Rev. B **38**(4), 2297–2311 (1988).
45. D. K. G. de Boer, "Influence of the roughness profile on the specular reflectivity of x rays and neutrons," Phys. Rev. B **49**(9), 5817–5820 (1994).
46. Y. Fujii, "Recent Analysis on Surface and Interface Roughness Using X-Ray Reflectivity," J. Mater. Sci. Nanotechnol. **6**, 202 (2018).
47. M. Wen, I. V. Kozhevnikov, and Z. Wang, "Reflection of X-rays from a rough surface at extremely small grazing angles," Opt. Express **23**(19), 24220 (2015).
48. M. Björck and G. Andersson, "GenX: an extensible X-ray reflectivity refinement program utilizing differential evolution," J. Appl. Crystallogr. **40**(6), 1174–1178 (2007).
49. G. Vignaud and A. Gibaud, "REFLEX: A program for the analysis of specular X-ray and neutron reflectivity data," J. Appl. Crystallogr. **52**(1), 201–213 (2019).
50. D. Ingerle, G. Pepponi, F. Meirer, P. Wobrauschek, and C. Streli, "JGIXA - A software package for the calculation and fitting of grazing incidence X-ray fluorescence and X-ray reflectivity data for the characterization of nanometer-layers and ultra-shallow-implants," Spectrochim. Acta, Part B **118**, 20–28 (2016).
51. A. Nelson, "Co-refinement of multiple-contrast neutron/X-ray reflectivity data using MOTOFIT," J. Appl. Crystallogr. **39**(2), 273–276 (2006).
52. A. R. J. Nelson and S. W. Prescott, "refnx: neutron and X-ray reflectometry analysis in Python," J. Appl. Crystallogr. **52**(1), 193–200 (2019).
53. D. G. Stearns, "The scattering of x rays from nonideal multilayer structures," J. Appl. Phys. **65**(2), 491–506 (1989).
54. A. Ulyanenkov, K. Omote, and J. Harada, "The genetic algorithm: refinement of X-ray reflectivity data from multilayers and thin films," Phys. B **283**(1-3), 237–241 (2000).
55. D. Attwood and A. Sakdinawat, "Scattering, Diffraction, and Refraction of Electromagnetic Radiation," in *X-Rays and Extreme Ultraviolet Radiation* (Springer, 2016), pp. 20–24.
56. B. L. Henke, E. M. Gullikson, and J. C. Davis, "X-Ray interactions: Photoabsorption, scattering, transmission, and reflection at E = 50-30,000 eV, Z=1-92," At. Data Nucl. Data Tables **54**(2), 181–342 (1993).
57. C. T. Chantler, "Detailed Tabulation of Atomic Form Factors, Photoelectric Absorption and Scattering Cross Section, and Mass Attenuation Coefficients in the Vicinity of Absorption Edges in the Soft X-Ray (Z = 30-36, Z = 60-89, E = 0.1-10 keV), Addressing Convergence Issues of Earlier Work," J. Phys. Chem. Ref. Data **29**(4), 597–1056 (2000).

OSA CONTINUUM

58. H. Akima, "A new method of interpolation and smooth curve fitting based on local procedures," J. Assoc. Comput. Mach. **17**(4), 589–602 (1970).
59. H. Akima, "A method of bivariate interpolation and smooth surface fitting based on local procedures," Commun. ACM **17**(1), 18–20 (1974).
60. F. N. Fritsch and R. E. Carlson, "Monotone Piecewise Cubic Interpolation," SIAM J. Numer. Anal. **17**(2), 238–246 (1980).
61. D. Kahaner, C. Moler, and S. Nash, *Numerical Methods and Software* (Prentice Hall, 1988).
62. K. Salamon, P. Dubček, G. Dražić, S. Bernstorff, and N. Radić, "Lateral inhomogeneities in W/C multilayer mirrors," Thin Solid Films **691**, 137611 (2019).